

# Transverse structural modulation in $\text{SrAl}_4$ and elucidation of its origin in the $\text{BaAl}_4$ family of compounds

Sitaram Ramakrishnan,<sup>1,\*</sup> Surya Rohith Kotla,<sup>2</sup> Hanqi Pi,<sup>3,4</sup> Bishal Baran Maity,<sup>5</sup>  
 Jia Chen,<sup>6,†</sup> Jin-Ke Bao,<sup>7</sup> Zhaopeng Guo,<sup>3,4</sup> Masaki Kado,<sup>1</sup> Harshit Agarwal,<sup>2</sup>  
 Claudio Eisele,<sup>2</sup> Minoru Nohara,<sup>1</sup> Leila Noohinejad,<sup>8</sup> Hongming Weng,<sup>3,9,4,‡</sup>  
 Srinivasan Ramakrishnan,<sup>10</sup> Arumugam Thamizhavel,<sup>5</sup> and Sander van Smaalen<sup>2,§</sup>

<sup>1</sup>*Department of Quantum Matter, AdSE,  
 Hiroshima University, Higashi-Hiroshima 739-8530, Japan*

<sup>2</sup>*Laboratory of Crystallography, University of Bayreuth, 95447 Bayreuth, Germany*

<sup>3</sup>*Beijing National Laboratory for Condensed Matter Physics,  
 Institute of Physics, Chinese Academy of Sciences, Beijing 100190, China*

<sup>4</sup>*School of Physics, University of Chinese Academy of Sciences, Beijing 100049, China*

<sup>5</sup>*Department of Condensed Matter Physics and Materials Science,  
 Tata Institute of Fundamental Research, Mumbai 400005, India*

<sup>6</sup>*Zhejiang Laboratory, Hangzhou 311121, China*

<sup>7</sup>*Department of Physics, Materials Genome Institute and  
 International Center for Quantum and Molecular Structures,  
 Shanghai University, Shanghai 200444, People's Republic of China*

<sup>8</sup>*P24, PETRA III, Deutsches Elektronen-Synchrotron DESY,  
 Notkestrasse 85, 22607 Hamburg, Germany*

<sup>9</sup>*Songshan Lake Materials Laboratory,  
 Dongguan, Guangdong 523808, China*

<sup>10</sup>*Department of Physics, Indian Institute of Science  
 Education and Research, Pune, 411008, India*

(Dated: September 28, 2024)

## Abstract

At ambient conditions  $\text{SrAl}_4$  adopts the  $\text{BaAl}_4$  structure type with space group  $I4/mmm$ . It undergoes a charge-density-wave (CDW) transition at  $T_{CDW} = 243$  K, followed by a structural transition at  $T_S = 87$  K. Temperature-dependent single-crystal X-ray diffraction (SXRD) leads to the observation of incommensurate superlattice reflections at  $\mathbf{q} = \sigma \mathbf{c}^*$  with  $\sigma = 0.1116$  at 200 K. The CDW has orthorhombic symmetry with the superspace group  $Fmmm(00\sigma)s00$ , where  $Fmmm$  is a subgroup of  $I4/mmm$  of index 2. Atomic displacements represent a transverse wave, and they are mainly along one of the diagonal directions of the  $I$ -centered unit cell. The orthorhombic phase realized in  $\text{SrAl}_4$  is analogous to that found in  $\text{EuAl}_4$ , albeit with the presence of higher order satellite reflections (up to  $m = 3$ ) and a shorter modulation wave vector. Electronic structure calculations and phonon calculations by density functional theory (DFT) have failed to reveal the mechanism of CDW formation. No clear Fermi surface nesting nor electron-phonon coupling nor the involvement of Dirac points could be established. However, DFT reveals that Al atoms dominate the density of states near the Fermi level, thus, corroborating the SXRD measurements.  $\text{SrAl}_4$  remains incommensurately modulated at the structural transition, where the symmetry lowers from orthorhombic to  $\mathbf{b}$ -unique monoclinic. The present work draws a comparison on the modulated structures of non-magnetic  $\text{SrAl}_4$  and magnetic  $\text{EuAl}_4$  elucidating their similarities and differences, and firmly establishing that although substitution of Eu to Sr plays little to no role in the structure, the transition temperatures are affected by the atomic sizes. We have identified a simple criterion, that correlates the presence of a phase transition with the interatomic distances. Only those compounds  $X\text{Al}_{4-x}\text{Ga}_x$  ( $X = \text{Ba}, \text{Eu}, \text{Sr}, \text{Ca}; 0 < x < 4$ ) undergo phase transitions, for which the ratio  $c/a$  falls within the narrow range  $2.51 < c/a < 2.54$ .

---

\* niranj002@gmail.com

† chenjia@zhejianglab.com

‡ hmweng@iphy.ac.cn

§ smash@uni-bayreuth.de

## I. INTRODUCTION

The manifestation of charge density waves (CDWs) was initially found to occur in quasi-one-dimensional (1D) electronic systems, like NbSe<sub>3</sub> and K<sub>0.3</sub>MoO<sub>3</sub> [1–3]. These compounds possess Fermi surfaces with co-planar sections that allow so-called Fermi surface nesting (FSN), thus explaining the stabilization of CDWs. The nesting vector of the periodic structure becomes the wave vector of the CDW in the valence bands, as well as the wave vector of the modulation of the atomic positions (periodic lattice distortion). Recent research has expanded the criteria for the occurrence of CDWs [4]. Materials need not support 1D or quasi-two-dimensional (2D) electron bands, but they can involve complex three-dimensional (3D) electronic system, if certain conditions are fulfilled. The mechanism of stabilization of CDW in these systems is provided by  $\mathbf{q}$ -dependent electron-phonon coupling (EPC). Several examples exist of 3D compounds with CDWs, which include CuV<sub>2</sub>S<sub>4</sub> [5–8],  $R_3\text{Co}_4\text{Sn}_{13}$  ( $R = \text{La}, \text{Ce}$ ) [9–11],  $R_5\text{Ir}_4\text{Si}_{10}$  ( $R = \text{Dy}, \text{Ho}, \text{Er}, \text{Yb}, \text{Lu}$ ) [12], Sm<sub>2</sub>Ru<sub>3</sub>Ge<sub>5</sub> [13, 14], TmNiC<sub>2</sub> [15, 16],  $R_2\text{Ir}_3\text{Si}_5$  ( $R = \text{Lu}, \text{Er}, \text{Ho}$ ) [17–19], CuIr<sub>2-x</sub>Cr<sub>x</sub>Te<sub>4</sub> [20], and kagome materials like AV<sub>3</sub>Sb<sub>5</sub> ( $A = \text{K}, \text{Rb}, \text{Cs}$ ) [21–26] and FeGe [27–29].

Compounds  $X\text{Al}_4/X\text{Ga}_4$  ( $X = \text{Eu}, \text{Ca}, \text{Sr}, \text{Ba}$ ) crystallize in the tetragonal BaAl<sub>4</sub> structure type with space group  $I4/mmm$ . These systems have attracted a lot of attention in the recent years, because of their properties as topological quantum materials [30–36]. EuAl<sub>4</sub>, containing divalent Eu, is a 3D CDW compound that also undergoes four successive antiferromagnetic (AFM) transitions below 20 K [37–41]. It has been reported to have a chiral spin structure and skyrmions [41, 42], similar to skyrmions reported in other divalent Eu-based systems, such as EuPtSi [43, 44]. A skyrmion state of magnetic order, and the non-trivial band topology were furthermore established by measurements of the topological Hall resistivity, the muon-spin rotation and relaxation ( $\mu\text{SR}$ ), and the magnetostriction [33, 35, 45]. Our recent investigation into the modulated structure of EuAl<sub>4</sub> reveals a breaking of the fourfold rotational symmetry, resulting in an orthorhombic  $Fmmm$  symmetry of the CDW state below 145 K. There is no evidence of a lattice distortion away from tetragonal symmetry. The reduction towards orthorhombic symmetry is brought about solely by the transverse CDW modulation in EuAl<sub>4</sub>.

Replacement of the divalent rare-earth element Eu by divalent alkaline earth metals Ba, Sr and Ca results in isostructural compounds. SrAl<sub>4</sub> and CaAl<sub>4</sub> undergo CDW transitions or

other structural transitions (STs). However,  $\text{BaAl}_4$  does not undergo any phase transition [32, 34]. Out of all the materials in the  $X\text{Al}_4$  series, the compound that is most similar to  $\text{EuAl}_4$  would be  $\text{SrAl}_4$ .  $\text{SrAl}_4$  exhibits a CDW transition at  $T_{CDW} = 243$  K, which is at a much higher temperature than the CDW transition of  $\text{EuAl}_4$  [46, 47]. Isostructural  $\text{CaAl}_4$  undergoes a ST at 443 K, which is at an even higher temperature than for  $\text{SrAl}_4$  [48].  $\text{SrAl}_4$  undergoes a second transition at  $T_S = 87$  K [46]. It was suggested that the symmetry of the low-temperature phase is monoclinic [46]. The mechanism of CDW formation in either  $\text{SrAl}_4$  or  $\text{EuAl}_4$  presently is not understood, as both compounds possess a complex 3D electronic structure [37, 46, 49].

Here, we present the results of temperature-dependent single-crystal x-ray diffraction (SXRD) experiments on  $\text{SrAl}_4$ . We find that the CDW transition is accompanied by a reduction in symmetry from tetragonal to orthorhombic, entirely analogous to  $\text{EuAl}_4$  [40], albeit with larger amplitudes for the modulation in  $\text{SrAl}_4$ . The network of Al atoms governs the CDW in  $\text{SrAl}_4$ , which is similar to the situation of  $\text{EuAl}_4$  [40]. This finding is supported by solid solution samples of isostructural  $\text{SrAl}_{4-x}\text{Si}_x$  and  $\text{SrAl}_{4-x}\text{Ge}_x$ , since the CDW is suppressed by the disorder at the Al site, and induces superconductivity in the case of Si-doping [50, 51]. From SXRD and physical properties measurements, we confirm that below 100 K  $\text{SrAl}_4$  undergoes a second phase transition that is characterized by a monoclinic lattice distortion, but across which the CDW modulation remains incommensurate. In this paper, we present the modulated crystal structure of  $\text{SrAl}_4$ , and we discuss the similarities and subtle differences in the CDWs of  $\text{SrAl}_4$  and  $\text{EuAl}_4$ . Furthermore, we establish that the value of  $c/a$  must be within the narrow range  $2.51 < c/a < 2.54$ , in order for the compound to undergo a phase transition. This allows us to predict whether new materials developed in this series could or could not undergo a CDW or structural transition.

## II. EXPERIMENTAL AND COMPUTATIONAL DETAILS

### A. Crystal growth

Single crystals of  $\text{SrAl}_4$  were grown by the Al self-flux method according to [46]. Crystals were grown at three places, using similar methods.

At the Lab. of Crystallography in Bayreuth, the elements strontium (Alfa Aesar, 99.95%



purity) and aluminium (Alfa Aesar, 99.9995%) were filled into an alumina crucible in the ratio 1:19. The crucible was sealed in an evacuated quartz-glass ampoule. It was heated to a temperature of 1173 K and held at this temperature for 2 hours. The crucible was then cooled to 823 K with a rate of 0.5 K/hour, at which point the crystals were separated from the molten metal by centrifugation. Small crystals were selected and annealed in vacuum for 72 hours at 723 K. The 1:4 stoichiometry of the product was confirmed by structure refinement against SXRD data. The resulting crystals A were used for the SXRD experiments.

At the Tata Institute in Mumbai, the elements were filled into an alumina crucible with the ratio 1:23. Crystal growth was at 1323 K for 24 hours, after which it was cooled to 973 K with a rate of 1 K/hour, followed by centrifugation. The longer growth time resulted in crystal B that is larger than crystal A. These crystals were employed without annealing for measurement of the specific heat. At the Department of Quantum Matter in Hiroshima, the same procedure was followed, resulting in crystal C that was used for the measurement of the electrical resistivity.

### **B. Single-crystal x-ray diffraction data collection**

SXRD experiments were performed at Beamline P24 of PETRA III at DESY in Hamburg, employing a four-circle Huber diffractometer with Euler geometry, and radiation of wavelength 0.50000 Å. The temperature of the crystal was controlled by a CRYOCOOL open-flow helium cryostat. Complete data sets were measured at temperatures of 293, 200, 120, 100, 75 and 20 K, covering all phases. Each run of data collection comprises 3640 frames, corresponding to a rotation of the crystal over 364 deg, which was repeated 10 times. These data were binned to a data set of 364 frames of 1 deg rotation and 10 s exposure time [52]. Further details are provided in the Supplemental Material [53].

### **C. Single-crystal x-ray diffraction data processing**

The EVAL15 software suite [54] was used for processing the SXRD data. Each temperature comprises two runs, one with and another without  $2\theta$  offset of the detector. The two runs were integrated separately, and subsequently merged in the module ANY of EVAL15. SADABS [55] was used for scaling and absorption correction with Laue symmetry  $4/mmm$

for the data measured at 293 K (periodic phase), with Laue symmetry  $mmm$  for the runs collected at 200, 120 and 100 K (CDW phase), and with Laue symmetry  $2/m$  (**b**-unique) at 20 K (low-temperature phase). The resulting reflection files were imported into the software JANA2006 [56, 57] for structure refinements. Tables I and II, and Tables S2–S4 in the Supplemental Material [53] give details of the analysis, crystallographic information, atomic coordinates and modulation amplitudes.

#### D. Density Functional Theory (DFT) Calculations

Density functional theory (DFT) calculations were performed for the tetragonal crystal structure of  $\text{SrAl}_4$  with space group of  $I4/mmm$ , employing the Vienna *ab initio* simulation package (VASP) [59]. The Projector-augmented-wave (PAW) method [60, 61] and generalized gradient approximations (GGA) [62] with Perdew-Burke-Ernzerhof (PBE) type pseudopotentials were chosen to deal with exchange-correlations.

The conventional unit cell was fully relaxed with a  $12 \times 12 \times 4$   $k$ -mesh sampling until the energy convergence tolerance fell below  $10^{-7}$  eV and the force was less than  $10^{-2}$  eV/Å. The cutoff energy of the plane-wave basis was chosen as 520 eV. The DFT optimized results are close to the experimental values (Table I). An  $18 \times 18 \times 18$   $k$ -mesh was implemented for the Brillouin zone (BZ) integral sampling of the primitive unit cell. The Fermi surface was calculated by using the WannierTools package [63] with tight-binding Hamiltonian constructed by the WANNIER90 code [64, 65], which is based on the maximally localized Wannier function (MLWF) method [66]. The bare charge susceptibility is carried out using a  $k$ -mesh of  $200 \times 200 \times 200$ . The phonon spectrum calculations were performed within the framework of density functional perturbation theory (DFPT) [67, 68] and the finite displacement method, implemented by the PHONOPY [69] package combined with VASP, and by Quantum ESPRESSO [70, 71].

#### E. Physical properties

The dc electrical resistivity was measured between 6 and 296 K, employing a standard four-probe method. The small size of the specimen prevented the identification of lattice directions, so that the single experimental run has resulted in  $\rho(T)$  along an unspecified,

TABLE I. Crystallographic data of crystal A of  $\text{SrAl}_4$  at 293 K (periodic phase) and 200 K (CDW phase).

Temperature (K)	293	200
Crystal system	Tetragonal	Orthorhombic
Space/Superspace group	$I4/mmm$	$Fmmm(00\sigma)s00$
No. [58]	139	69.1.17.2
$a$ (Å)	4.4893(2)	6.3326(4)
$b$ (Å)	4.4893	6.3331(5)
$c$ (Å)	11.2764(5)	11.2541(5)
Volume (Å <sup>3</sup> )	227.26(3)	451.35(4)
Wavevector $\mathbf{q}$	-	0.1116(2) $\mathbf{c}^*$
$Z$	2	4
Wavelength (Å)	0.50000	0.50000
Detector distance (mm)	260	260
$2\theta$ -offset (deg)	0, 25	0, 25
$\chi$ -offset (deg)	-60	-60
Rotation per image (deg)	1	1
$(\sin(\theta)/\lambda)_{max}$ (Å <sup>-1</sup> )	0.746821	0.745874
Absorption, $\mu$ (mm <sup>-1</sup> )	4.844	4.878
$T_{min}, T_{max}$	0.3118, 0.3522	0.3121, 0.3515
Criterion of observability	$I > 3\sigma(I)$	$I > 3\sigma(I)$
No. of reflections measured,		
( $m = 0$ )	630	493
( $m = 1$ )	-	969
( $m = 2$ )	-	971
Unique reflections (obs/all),		
( $m = 0$ )	137/139	197/211
( $m = 1$ )	-	323/392
( $m = 2$ )	-	94/403
$R_{int}$ ( $m = 0$ ) (obs/all)	0.0241/0.0241	0.0229/0.0229
$R_{int}$ ( $m = 1$ ) (obs/all)	-	0.0979/0.0978
$R_{int}$ ( $m = 2$ ) (obs/all)	-	0.0845/0.1010
No. of parameters	9	25
$R_F$ ( $m = 0$ ) (obs)	0.0144	0.0276
$R_F$ ( $m = 1$ ) (obs)	-	0.0452
$R_F$ ( $m = 2$ ) (obs)	-	0.1463
$wR_F$ ( $m = 0$ ) (all)	0.0186	0.0306
$wR_F$ ( $m = 1$ ) (all)	-	0.0612
$wR_F$ ( $m = 2$ ) (all)	-	0.1767
$wR_F$ all (all)	0.0186	0.0494
GoF (obs/all)	1.28/1.27	1.69/1.35
$\Delta\rho_{min}, \Delta\rho_{max}$ (e Å <sup>-3</sup> )	-0.29, 0.47	-1.89, 3.89

TABLE II. Amplitudes of the modulation functions of crystal A at 200 K for superspace group  $Fmmm(00\sigma)s00$ . The relative coordinates,  $x$ ,  $y$  and  $z$  of the basic position are also specified. Values of modulation amplitudes have been multiplied by the corresponding lattice parameter, in order to obtain values in Å.

Atom	Sr	Al1	Al2
$x$	0	0.25	0
$y$	0	0.25	0
$z$	0	0.25	0.38360(12)
$A_{1,x} a$ (Å)	0.2323(9)	0.2274(25)	0.2325(24)
$A_{1,y} b$ (Å)	0	0	0
$A_{1,z} c$ (Å)	0	0	0
$B_{1,x} a$ (Å)	0	0	0.0661(18)
$B_{1,y} b$ (Å)	0	0.0731(24)	0
$B_{1,z} c$ (Å)	0	0	0
$A_{2,x} a$ (Å)	0	0	0
$A_{2,y} b$ (Å)	0	0	0
$A_{2,z} c$ (Å)	0.0084(15)	0.0058(40)	0.0015(36)
$B_{2,x} a$ (Å)	0	0	0
$B_{2,y} b$ (Å)	0	0	0
$B_{2,z} c$ (Å)	0	0	-0.0003(37)
$A_{3,x} a$ (Å)	0.0230(18)	0.0218(51)	0.0137(45)
$A_{3,y} b$ (Å)	0	0	0
$A_{3,z} c$ (Å)	0	0	0
$B_{3,x} a$ (Å)	0	0	0.0161(44)
$B_{3,y} b$ (Å)	0	-0.0112(86)	0
$B_{3,z} c$ (Å)	0	0	0

general direction. Basically, the temperature dependence of the electrical resistivity confirms the data reported in Ref. [46]. The present resistivity data are given in Section S5 of the Supplemental Material. A commercial physical property measurement system (PPMS, Quantum Design, USA) was used for measuring the specific heat data in a heating run.

### III. RESULTS AND DISCUSSION

#### A. The orthorhombic CDW phase

$\text{SrAl}_4$  has been reported to undergo two phase transitions: one at  $T_{CDW} = 243$  K and another below 90 K [46]. Cooling the crystal from 293 to 200 K revealed superlattice reflections with  $\mathbf{q} = 0.1116(2) \mathbf{c}^*$  at 200 K, similar to the diffraction of isostructural  $\text{EuAl}_4$  below 145 K [38, 40]. The data measured at 200 K (incommensurate CDW phase) could be refined successfully (Table I). Like for  $\text{EuAl}_4$  [38, 40], we do not observe any lattice distortion within the CDW phase, thus preserving the tetragonal lattice symmetry for the basic structure.

In order to elucidate the modulated CDW structure at 200 K, we have tested different superspace groups as symmetry of the crystal structure (See Tables S2 and S3 in the Supplemental Material [53]). The three candidate models are based on symmetries  $I4/mmm$  (model A) and its maximal orthorhombic subgroups  $Immm$  (model B) and  $Fmmm$  (model C). The latter symmetry resulted in the best fit to the SXRD data (Section S2 in the Supplemental Material [53]). The analysis thus gave model C with superspace symmetry  $Fmmm(00\sigma)s00$  as structure model for the incommensurately modulated CDW state of  $\text{SrAl}_4$ .

Although the modulated crystal structure of  $\text{SrAl}_4$  below 243 K is isostructural to that of  $\text{EuAl}_4$  below 145 K, there are some differences. Unlike  $\text{EuAl}_4$ , we have observed higher order superlattice reflections in the SXRD of  $\text{SrAl}_4$  (Fig. 1). Consequently, the modulation functions include higher-order harmonic amplitudes. Structure refinements indicate a significantly better fit to the satellite reflections for model CII with up to 3<sup>rd</sup>-order harmonics than for model CI with up to 2<sup>nd</sup>-order harmonics (Table III). Therefore, we selected model CII with up to 3<sup>rd</sup>-order harmonics in the modulation functions for further analysis (Tables I and II, and Table S4 in [53]).

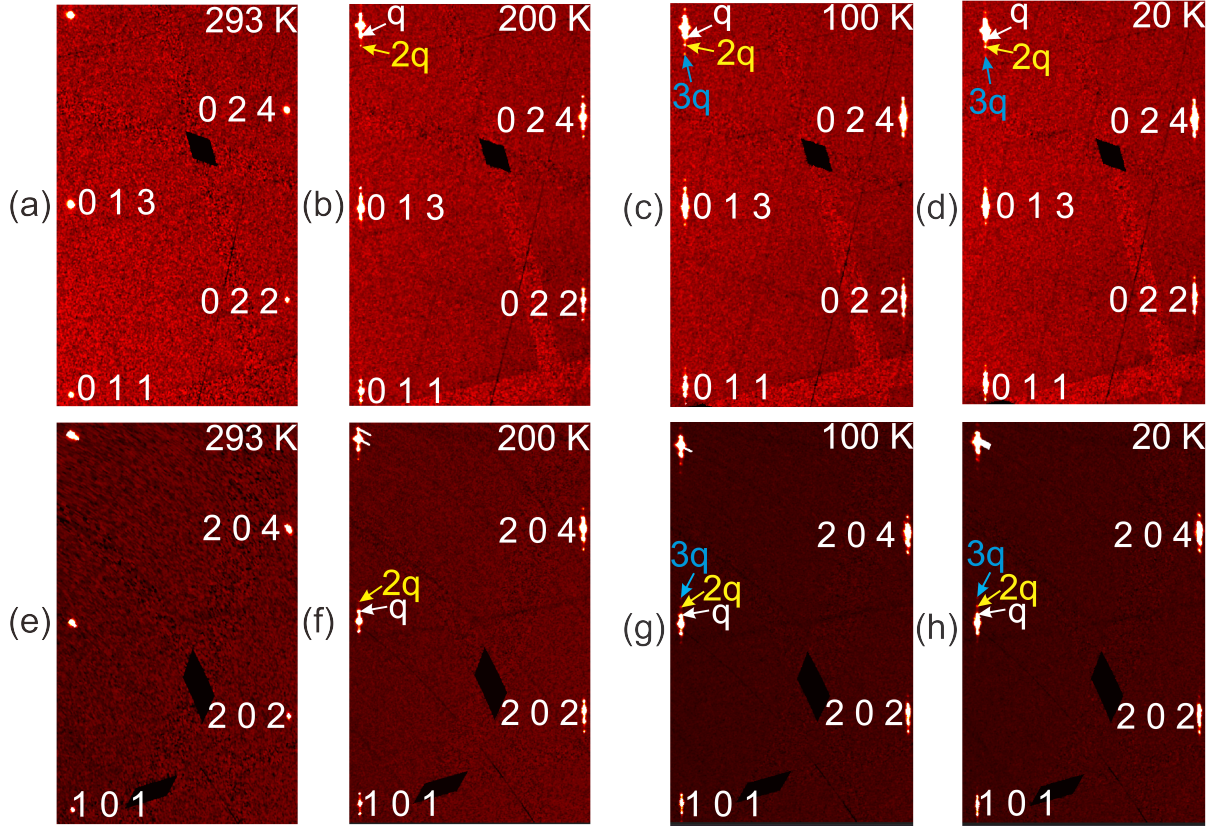


FIG. 1. Excerpts of the reciprocal layers of diffraction for (a)–(d)  $(0kl)$  and (e)–(f)  $(h0l)$ , as reconstructed from the measured SXRD data [72]. (a)–(d) and (e)–(f) display scattering for temperatures of 293, 200, 100 and 20 K, as indicated. Indices are given for selected main reflections. Selected satellite reflections are indicated by arrows. Up to  $3^{rd}$ -order satellites are visible at 20 and 100 K. Dark gaps are due to insensitive pixels between the active modules of the PILATUS3X CdTe 1M detector.

Upon further cooling below 200 K, the length of the modulation wave vector gradually shrinks [Fig. 2(d)]. As a consequence, main reflections and nearby satellite reflections are not always resolved at 120 K and below (compare the streaky maxima in Fig. 1). A reliable extraction was not possible of the values for the integrated intensities of individual Bragg reflections for  $T < 120$  K.

TABLE III. Fit to the SXRD data at 200 K for different models with superspace group  $Fmmm(00\sigma)s00$ . Model CI incorporates up to  $2^{nd}$ -order harmonics, and model CII incorporates up to  $3^{rd}$ -order harmonics. Criterion of observability:  $I > 3\sigma(I)$ .

Model	CI	CII
$R_F(m = 0)(\text{obs/all})$ (%)	2.76/2.80	2.76/2.80
$R_F(m = 1)(\text{obs/all})$ (%)	5.04/5.17	4.52/4.65
$R_F(m = 2)(\text{obs/all})$ (%)	18.70/25.42	14.63/19.69
No. of unique reflections		
$m = 0$ (obs/all)	197/211	197/211
$m = 1$ (obs/all)	323/392	323/392
$m = 2$ (obs/all)	94/403	94/403
No. of parameters	20	25

## B. Location of the CDW

$\text{SrAl}_4$  is isostructural to  $\text{EuAl}_4$  with a tetragonal crystal structure at room temperature [73], that is preserved as basic structure at lower temperatures (Fig. 3).

The modulation amplitudes exhibit the following features in comparison to those of  $\text{EuAl}_4$ . Firstly, the largest modulation has an amplitude of 0.23 Å along  $\mathbf{a}$  for all atoms, which is about twice the value of 0.12 Å for the atoms of  $\text{EuAl}_4$  (Table II and [40]). In addition,  $\text{SrAl}_4$  features  $3^{rd}$ -order harmonic amplitudes of values of about 10% of the  $1^{st}$ -order harmonic coefficients.

Secondly, exclusively the atom Al1 has a modulation along  $\mathbf{b}$  of amplitude 0.073 Å, which is only 17% larger than in  $\text{EuAl}_4$ . Again, this modulation has a  $3^{rd}$ -order harmonic contribution of about 15% of the  $1^{st}$ -order harmonic, which is in antiphase with the  $1^{st}$ -order harmonic and thus responsible for the obviously anharmonic shape of the Al1–Al1 distance along the incommensurate coordinate  $t$  (Fig. 4). The  $2^{nd}$ -order harmonic amplitudes attain values close to zero.

The shortest Al1–Al1 contacts are the only short intermetallic distances with a significant variation with the phase of the modulation. This is furthermore illustrated by Table IV, where the modulations of interatomic distances are given for both  $\text{EuAl}_4$  and  $\text{SrAl}_4$ . Apart

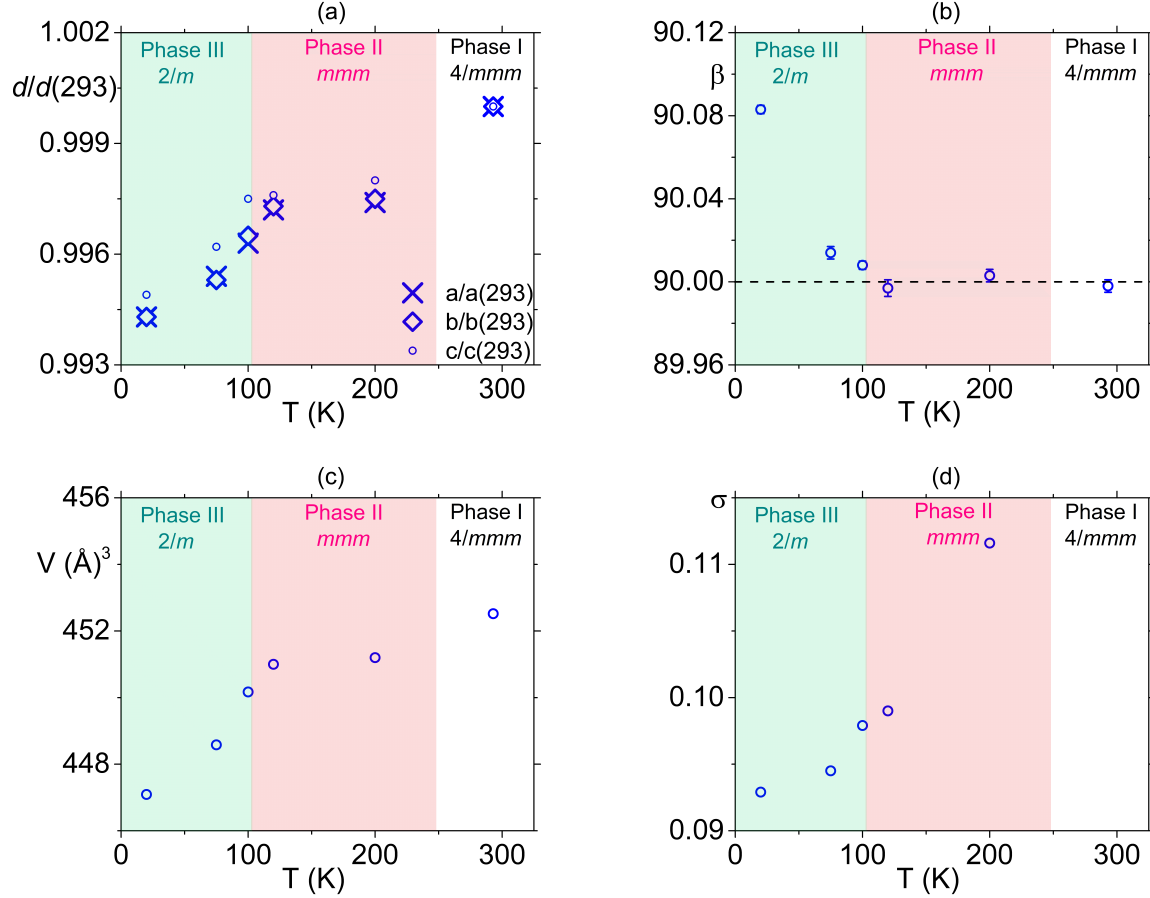


FIG. 2. Lattice parameters and modulation wave vector within the temperature range 20–293 K. (a) Lattice parameters ( $F$ -centered setting) relative to their values at  $T = 293$  K, with  $a(293) = 6.3488(3)$ ,  $b(293) = 6.3488$  and  $c(293) = 11.2764(3)4$   $\text{\AA}$ . (b) The lattice parameter  $\beta$  in deg. (c) Volume of the unit cell. (d) Component  $\sigma$  of  $\mathbf{q} = (0, 0, \sigma)$ , which remains incommensurate down to 20 K.

from a general expansion of the latter, variations of distances due to the modulations are nearly equal in the two compounds. Therefore, in analogy to  $\text{EuAl}_4$ , we conclude that the Al1 atoms govern the formation of the CDW.

### C. Criteria for the formation of CDW in $\text{BaAl}_4$ type compounds

Only a few of the isostructural compounds  $X\text{Al}_{4-x}\text{Ga}_x$  ( $X = \text{Ba}, \text{Eu}, \text{Sr}, \text{Ca}; 0 < x < 4$ ) undergo phase transitions. First, it is noticed that chemical disorder tends to suppress a CDW transition, if the disorder is at sites carrying the CDW. The transition temperature is



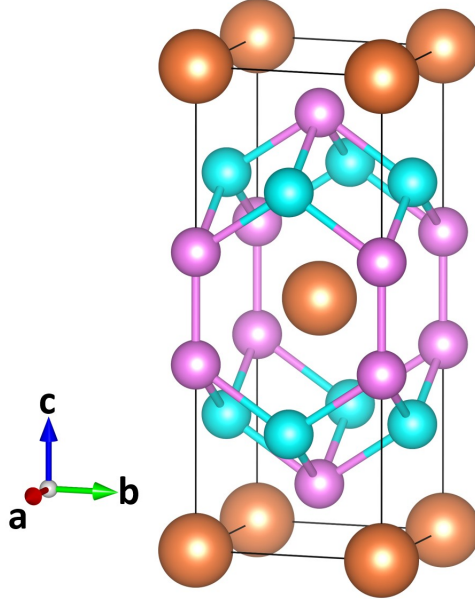


FIG. 3. Crystal structure of  $\text{SrAl}_4$  with space group  $I4/mmm$  in the periodic phase at 293 K. Depicted is the  $I$ -centered unit cell with basis vectors  $\mathbf{a}_I$ ,  $\mathbf{b}_I$  and  $\mathbf{c}_I$ . Orange spheres correspond to the Sr atoms; green-bluish spheres represent Al1 atoms; and pink spheres stand for Al2 atoms. Shortest interatomic distances are:  $d[\text{Sr-Sr}] = 4.4893(4) \text{ \AA}$ ,  $d[\text{Al1-Al1}] = 3.1774(2) \text{ \AA}$ ,  $d[\text{Al2-Al1}] = 2.7034(6) \text{ \AA}$  and  $d[\text{Al2-Al2}] = 2.6250(15) \text{ \AA}$ . The crystal structure was drawn using VESTA [74].

lowered upon increasing doping, while a few percent of doping can be sufficient to completely suppress the CDW transition [76, 77]. The sensitivity of the CDW for chemical disorder explains the absence of CDW transitions in  $\text{EuAl}_{4-x}\text{Ga}_x$  ( $0 < x < 4$ , except  $x = 0$  and  $x = 2$ ) [31], and the absence of CDW transitions in  $\text{SrAl}_{4-x}\text{Si}_x$  and  $\text{SrAl}_{4-x}\text{Ge}_x$  [50, 51].

Thus, restricting the analysis to compounds  $X\text{Al}_{4-x}\text{Ga}_x$  with  $x = 0, 2$  or  $4$ , we make the observation that structural and CDW phase transitions take place in compounds that have the ratio  $c/a$  within a narrow range:  $2.51 < c/a < 2.54$  (Fig. 5).  $\text{EuGa}_4$  has a CDW phase transition for pressures exceeding 2 GPa [37]. One might then speculate, that the ratio  $c/a$  of  $\text{EuGa}_4$  at high pressures will be within the critical range (Fig. 5). This criterion is useful to predict CDWs in new compounds of this family. At present there is no information regarding whether  $\text{SrAl}_2\text{Ga}_2$  exhibits CDW or other structural transitions.

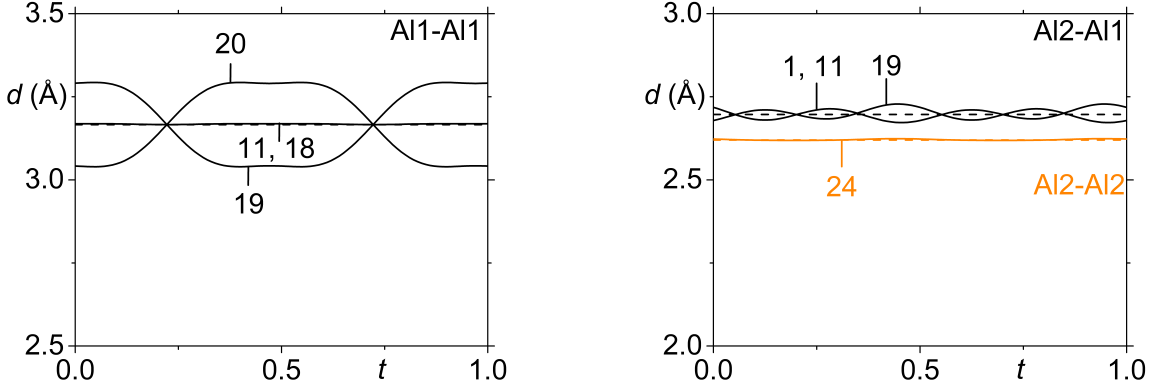


FIG. 4.  $t$ -Plot of interatomic distances ( $\text{\AA}$ )  $d[\text{Al1-Al1}]$ ,  $d[\text{Al2-Al1}]$  and  $d[\text{Al2-Al2}]$  at 200 K, where the first atom is the central atom.  $t$ -Plots display interatomic distances as a function of the phase  $t$  of the modulation wave [75]. In case of multiple curves, each value of  $t$  gives the distances from a central atom towards its neighboring atoms. The number on each curve is the number of the symmetry operator that is applied to the second atom of the bond pair. Symmetry operators are listed in Table S6 in the supporting information.

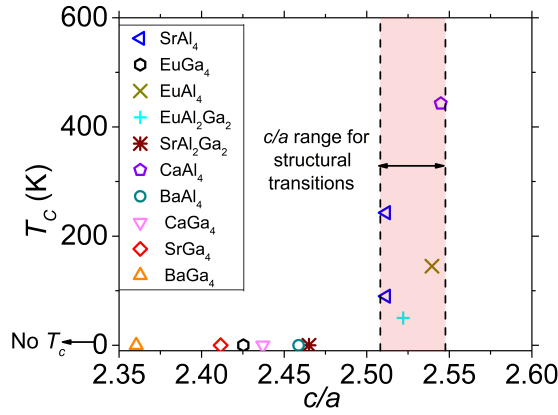


FIG. 5. Value of  $T_c = T_S$  or  $T_{CDW}$  as a function of the ratio  $c/a$  for eleven compounds  $X\text{Al}_{4-x}\text{Ga}_x$ . Only four compounds undergo phase transitions.

#### D. Evidence of monoclinic distortion below 100 K

The orthorhombic phase is realized through the orthorhombic symmetry of the CDW modulation displacements (Table II), while the lattice and basic structure remain tetragonal

TABLE IV. Selected structural information on the CDW phases of  $\text{EuAl}_4$  [40] and  $\text{SrAl}_4$  (present work). The Crystal structures have superspace group  $Fmmm(00\sigma)s00$ .

Compound	$\text{EuAl}_4$	$\text{SrAl}_4$
$T_{CDW}$ (K)	145	243
$T$ (K)	70	200
$a$ (Å)	6.1992(4)	6.3326(4)
$b$ (Å)	6.2001(4)	6.3331(5)
$c$ (Å)	11.1477(3)	11.2541(5)
$V$ (Å <sup>3</sup> )	428.47(4)	451.34(6)
$\sigma$	0.1781(3)	0.1116(2)
Distance Al1–Al1 <sup>a,b</sup> along <b>a</b>		
max (Å)	3.102(3)	3.169(11)
min (Å)	3.100(3)	3.166(11)
avg (Å)	3.101(2)	3.168(5)
Distance Al1–Al1 <sup>c,d</sup> along <b>b</b>		
max (Å)	3.224(3)	3.293(16)
min (Å)	2.976(3)	3.040(16)
avg (Å)	3.101(2)	3.168(8)
Distance Al2–Al1 <sup>e,f,g,h</sup>		
max (Å)	2.669(2)	2.728(8)
min (Å)	2.651(2)	2.672(8)
avg (Å)	2.659(2)	2.698(8)
Distance Al2–Al2 <sup>i</sup>		
max (Å)	2.567(3)	2.624(6)
min (Å)	2.566(2)	2.619(6)
avg (Å)	2.567(2)	2.621(6)

Given are the maximum (max), minimum (min) and average (avg) interatomic distances, with the symmetry operation applied to the second atom.

<sup>a,b</sup> Symmetry codes for Al1–Al1:  $(-x + 1, -y + 1/2, -z + 1/2)$ ,  $(-x + 1/2, -y, -z + 1/2)$

<sup>c,d</sup> Symmetry codes for Al1–Al1:  $(-x + 1/2, -y + 1, -z + 1/2)$ ,  $(x, y + 1/2, z - 1/2)$

<sup>e,f,g,h</sup> Symmetry codes for Al2–Al1:  $(x, y, z)$ ,  $(x - 1/2, y - 1/2, z)$ ,  $(-x, -y + 1/2, -z + 1/2)$ ,  $(-x + 1/2, -y, -z + 1/2)$

<sup>i</sup> Symmetry code for Al2–Al2:  $(-x, y, -z + 1)$

(Fig. 2 and Table S4). The structural transition at  $T_S = 87$  K is accompanied by a lattice distortion. In particular, we find the angle  $\beta$  to be different from 90 deg within the low-temperature phase [Fig. 2(b)]. These values indicate that the low-temperature phase is **b**-unique monoclinic, in agreement with Nakamura *et al.* [46].

The structural phase transition leads to a twinned crystal, such that the monoclinic lattice distortion is visible as split reflections in  $q$ -scans along the direction of  $\mathbf{c}^*$ . For example, for the reflection  $(0\ 2\ 4)$ , a secondary peak appears below 100 K between the main reflection and first-order satellite (Fig. S1 in the Supplemental Material [53]). Furthermore, these  $q$ -scans

show that the incommensurate CDW satellite reflections persist into the low-temperature phase. Across  $T_S$ , they continue to grow in intensity and the length of  $\mathbf{q}$  continues to decrease [Fig. 2(d)].

Due to overlap between main and satellite reflections, as it is the result of the short modulation wave vector [Fig. 2(d)], structure refinements failed. However, measured intensities are of sufficient quality to distinguish between tetragonal, orthorhombic and monoclinic symmetries on the basis of  $R_{int}$  values for averaging equivalent reflections. These quantities clearly favor monoclinic,  $\mathbf{b}$ -unique symmetry for the low-temperature phase (Table V).

TABLE V. Comparison of models on basis of SSG and  $R_{int}$  at 20 K. Criterion of observability:  $I > 3\sigma(I)$

SSG	$I4/mmm(00\sigma)0000$	$Fmmm(00\sigma)s00$	$F2/m(\sigma_10\sigma_2)00$
$R_{int} (m = 0)(\text{obs/all})\%$	5.07/5.07	3.78/3.79	1.62/1.62
$R_{int} (m = 1)(\text{obs/all})\%$	38.47/38.47	30.86/30.86	5.33/5.35
$R_{int} (m = 2)(\text{obs/all})\%$	64.42/64.43	38.41/38.41	6.23/9.16
Unique ( $m = 0$ ) (obs/all)	46/50	138/202	255/344
Unique ( $m = 1$ ) (obs/all)	75/106	317/381	567/732
Unique ( $m = 2$ ) (obs/all)	24/108	204/405	296/741

### E. Electronic Band Structure and Phonons

We have calculated the electronic structure and topological properties of  $\text{SrAl}_4$  for its  $I4/mmm$  crystal structure. Dispersion relations along high-symmetry directions within the Brillouin zone are given in Fig. 6(a,b). In the absence of SOC, several band crossings exist between the highest valence band and the lowest conduction band near the Fermi level [Fig. 6(a)]. When the SOC is considered, most band crossings are gapped, except one crossing along the line M- $\Gamma$  [Fig. 6(b)]. Unfortunately, it appears at around  $E = 0.2$  eV above the Fermi level, which is not easy to find experimentally.

Using the software IRVSP [78], we found that these two bands belong to the irreducible representations of point group  $4mm$ , marked LD6 (green line) and LD7 (orange line), respectively [Fig. 6(b)]. This indicates that the band crossing is a topologically protected Dirac

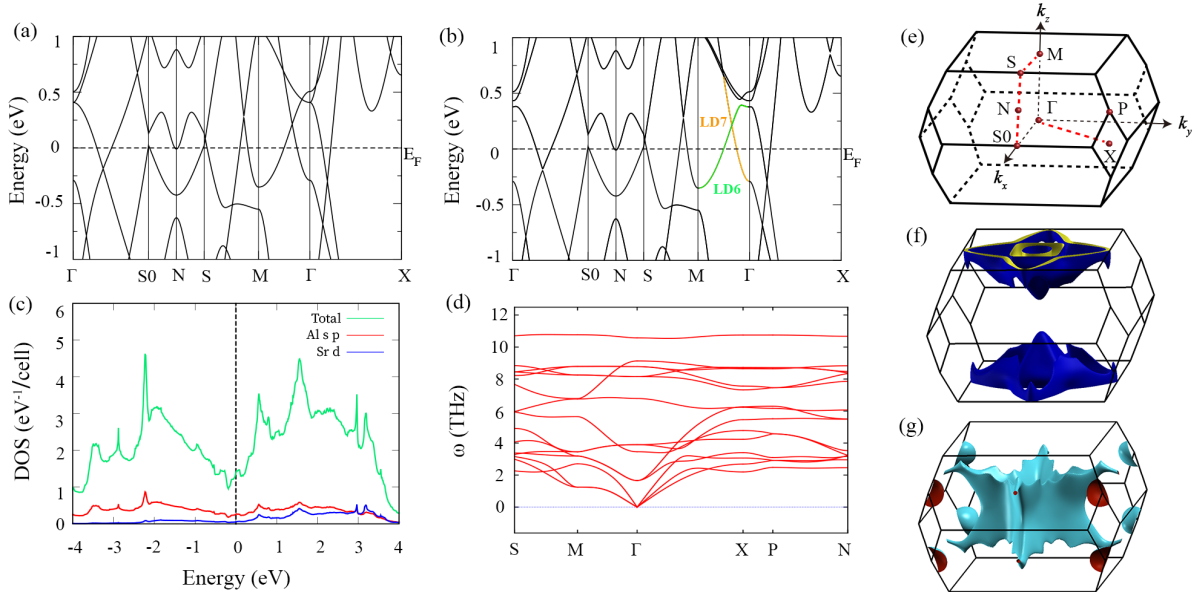


FIG. 6. The bulk band structures of the tetragonal crystal structure  $I4/mmm$  of  $\text{SrAl}_4$ . (a) Electronic band structure along high-symmetry directions, as obtained without SOC. (b) Electronic band structure calculated with SOC. The dashed lines indicate the Fermi energy,  $E_F$ . All band crossings are gapped out by SOC, except the crossing of two bands along the M- $\Gamma$  direction, labeled LD6 (green) and LD7 (orange). (c) The density-of-states (DOS) of the primitive unit cell with SOC. The green line gives the total DOS; the red line gives the contributions of  $2s$  and  $2p$  orbitals of Al; and the blue line stands for contributions of the  $3d$  orbital of Sr  $d$ . (d) Phonon dispersion relations obtained by DFPT calculations for a  $3 \times 3 \times 2$  supercell of the conventional unit cell. (e) First Brillouin zone of the primitive unit cell. (f) Hole pockets, and (g) electron pockets of the Fermi surface.

point. It follows that  $\text{SrAl}_4$  is a Dirac nodal line semimetal without SOC and becomes a Dirac semimetal when the SOC is considered, like  $\text{EuAl}_4$  [37, 40].

The total and atom-projected density of states (DOS) near  $E_F$  are given in Fig. 6(c). They reveal that Al states (red line) dominate the DOS near the Fermi level. This observation parallels the situation observed for  $\text{EuAl}_4$  [40]. Consequently, it is plausible to infer that the CDW is associated with the Al atoms rather than the Sr atoms.

Additional information on the mechanism of CDW formation in  $\text{SrAl}_4$  might be obtained from the phonon dispersion relations and the Fermi surface. Figure 6(d) shows the phonon dispersion relations, as computed with aid of a  $3 \times 3 \times 3$  supercell of the primitive basic

cell, containing 135 atoms. Density functional perturbative theory (DFPT) [67, 68] was used with a  $4 \times 4 \times 2$   $k$ -mesh. No imaginary frequencies or soft modes can be identified, indicating that electron-phonon coupling (EPC) is too weak to induce a CDW transition. This result is further checked by the application of alternative computational methods. For the same  $3 \times 3 \times 3$  supercell, phonon dispersion relations were computed by the finite displacement method. Small imaginary frequencies were obtained on the line M- $\Gamma$ , when a  $3 \times 3 \times 3$   $k$ -mesh was used for the computation (see Fig. S10(a) in the Supplementary Material [53]). These imaginary frequencies are eliminated, when the number of  $k$ -points is increased toward to  $5 \times 5 \times 5$  (Fig. S10(b) in [53]). The software Quantum Espresso [70, 71] leads to the same conclusion [compare Figs. S10(b),(c) and Fig. 6(d)].

The Fermi surface of SrAl<sub>4</sub> comprises hole pockets centered on the point M [Fig. 6(f)], as well as electron pockets surrounding  $\Gamma$  and those centered on point P [Fig. 6(g)]. To further check whether Fermi surface nesting (FSN) could be responsible for this CDW, the bare charge susceptibility [79] was calculated, employing a  $k$ -mesh of  $200 \times 200 \times 200$ , and considering four conduction bands and four valence bands near the Fermi level,

$$\begin{aligned} \lim_{\omega \rightarrow 0} \chi_0''(\mathbf{q}, \omega)/\omega &= \sum_{n, n', \mathbf{k}} \delta(\varepsilon_{n, \mathbf{k}} - \varepsilon_F) \delta(\varepsilon_{n', \mathbf{k} + \mathbf{q}} - \varepsilon_F) \\ \chi_0'(\mathbf{q}) &= \sum_{n, n', \mathbf{k}} \frac{f(\varepsilon_{n, \mathbf{k}}) - f(\varepsilon_{n', \mathbf{k} + \mathbf{q}})}{\varepsilon_{n, \mathbf{k}} - \varepsilon_{n', \mathbf{k} + \mathbf{q}}}, \end{aligned} \quad (1)$$

where  $f(\varepsilon_{n, \mathbf{k}})$  is the Fermi-Dirac distribution function. The real and imaginary components of the bare charge susceptibility of the SrAl<sub>4</sub> on the  $k_z = 0.11 c^*$  plane are depicted as a function of wave vector  $\mathbf{q}$  in Fig. S11(a,c) in the Supplemental Material [53]. Both components exhibit peak values at the center. We further conducted additional calculations of the bare charge susceptibility along the  $k_z$  line with  $k_x = k_y = 0$ , and present the outcomes in Fig. S11(b,d). The real component shows a peak near the experimentally observed  $\mathbf{q}$  vector, whereas the imaginary part does not. This discrepancy indicates that Fermi surface nesting (FSN) is insufficient to induce the charge density wave (CDW) in SrAl<sub>4</sub>. These conclusions are consistent with the analysis previously done for SrAl<sub>4</sub> and EuAl<sub>4</sub> [37, 40, 46], concluding that a clear mechanism of the CDW cannot be determined directly.

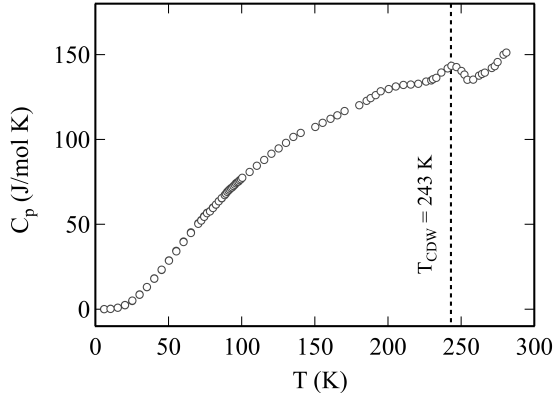


FIG. 7. Temperature dependence of the specific heat  $C_p$  of  $\text{SrAl}_4$  for 3–280 K, as obtained during heating of the sample. A broad maximum is observed at  $T_{CDW} = 243$  K (indicated by a vertical dashed line). No anomaly could be detected near the second structure transition at  $T_S = 87$  K.

### F. Specific heat

The temperature dependence of the specific heat ( $C_p$ ) shows a broad maximum at  $T_{CDW}$  of magnitude  $\Delta C_p \approx 12 \text{ J mol}^{-1} \text{ K}^{-1}$  (Fig. 7), which is more pronounced than observed for  $\text{EuAl}_4$  [40]. The measured  $C_p(T)$  data do not show any anomaly at the temperature  $T_S$  of the structural phase transition (Fig. 7). This might be related to the relaxation method of measurement, as employed in the PPMS instrument [80]. Alternatively, the absence of a transition at  $T_S$  might be the result of the presence of lattice defects in as-grown material, as previously described for  $\text{CuV}_2\text{S}_4$  [8].

## IV. CONCLUSIONS

From SXR D experiments and the physical properties measurements we confirm that  $\text{SrAl}_4$  undergoes two phase transitions. At  $T_{CDW} = 243$  K a CDW transition takes place, at which the crystal symmetry is lowered from tetragonal to orthorhombic. For the structural transition at  $T_S = 87$  K, SXR D unambiguously shows that the low-temperature phase is **b**-axis monoclinic, and that the CDW is virtually unaffected by this transition.

Replacement of non-magnetic Sr from magnetic Eu has a minimal role in the crystal structure, but does affect the value of  $T_{CDW}$ , which can be explained by different atomic radii of Sr and Eu. This idea has been expanded towards  $\text{CaAl}_4$  and  $\text{BaAl}_4$ . More generally,

isostructural compounds with the tetragonal  $\text{BaAl}_4$  structure type exist for  $X\text{Al}_{4-x}\text{Ga}_x$  ( $X = \text{Ba}, \text{Eu}, \text{Sr}, \text{Ca}; 0 < x < 4$ ). We could show that only those compounds undergo phase transitions for which  $c/a$  falls within the narrow range  $2.51 < c/a < 2.54$  (Fig. 5), while CDW transitions may be found only in case of the lack of chemical disorder, *i.e.* only in compounds with  $x = 0, 2$ , or  $4$ .

Both SXR and electronic band structure calculations support the interpretation that the network of Al atoms is the key contribution to CDW formation, much like in  $\text{EuAl}_4$ . The system possibly possesses a non-trivial band topology and a complex Fermi surface, preventing the mechanism of CDW formation to be simply uncovered in  $\text{SrAl}_4$ .

We surmise that it may be possible to realise multiple phases in  $\text{EuAl}_4$ , as the latter is proposed to go towards monoclinic symmetry in the AFM phases [40]. For  $\text{CaAl}_4$  there may exist an intermediary orthorhombic phase between its tetragonal and monoclinic phases.

## ACKNOWLEDGMENTS

Single crystals of  $\text{SrAl}_4$  were grown by Kerstin Küspert at the Laboratory of Crystallography in Bayreuth, and by Ruta Kulkarni at the Tata Institute of Fundamental Research in Mumbai. We thank Yilin Wang, Chao Cao, Simin Nie and Zhijun Wang for useful discussions about theoretical calculations and exploration of CDW mechanisms. We thank M. Tolkieln and C. Paulmann for their assistance at Beamline P24. We acknowledge DESY (Hamburg, Germany), a member of the Helmholtz Association HGF, for the provision of experimental facilities. Parts of this research were carried out at PETRA III, using beamline P24. Beamtime was allocated for proposal I-20210805. J. Chen is supported by China Postdoctoral Science Foundation (No. 2022M722916). This work was partly supported by JSPS KAKENHI Grant Numbers JP21K03448 and JP23H04630. The research at the University of Bayreuth has been funded by the Deutsche Forschungsgemeinschaft (DFG, German Research Foundation)–406658237.

- 
- [1] G. Grüner, The dynamics of charge-density waves, *Rev. Mod. Phys.* **60**, 1129 (1988).
  - [2] G. Grüner, *Charge Density Waves in Solids* (Addison-Wesley, Reading, Massachusetts, 1994).
  - [3] P. Monceau, Electronic crystals: an experimental overview, *Adv. Phys.* **61**, 325 (2012).



- [4] X. Zhu, J. Guo, J. Zhang, and E. W. Plummer, Misconceptions associated with the origin of charge density waves, *Adv. Phys.: X* **2**, 622 (2017).
- [5] R. M. Fleming, F. J. DiSalvo, R. J. Cava, and J. V. Waszczak, Observation of charge-density waves in the cubic spinel structure  $\text{CuV}_2\text{S}_4$ , *Phys. Rev. B* **24**, 2850 (1981).
- [6] S. Kawaguchi, Y. Kubota, N. Tsuji, J. Kim, K. Kato, M. Takata, and H. Ishibashi, Structural analysis of spinel compound  $\text{CuV}_2\text{S}_4$  with incommensurate charge-density wave, *J. Phys. Conf. Ser.* **391**, 012095 (2012).
- [7] H. Okada, K. Koyama, and K. Watanabe, Two-step structural modulations and Fermi liquid state in spinel compound  $\text{CuV}_2\text{S}_4$ , *J. Phys. Soc. Jpn* **73**, 3227 (2004).
- [8] S. Ramakrishnan, A. Schönleber, C. B. Hübschle, C. Eisele, A. M. Schaller, T. Rekiş, N. H. A. Bui, F. Feulner, S. van Smaalen, B. Bag, S. Ramakrishnan, M. Tolkieln, and C. Paulmann, Charge density wave and lock-in transitions of  $\text{CuV}_2\text{S}_4$ , *Phys. Rev. B* **99**, 195140 (2019).
- [9] A. Slebarski and J. Goraus, Electronic structure and crystallographic properties of skutterudite-related  $\text{Ce}_3\text{M}_4\text{Sn}_{13}$  and  $\text{La}_3\text{M}_4\text{Sn}_{13}$  ( $M = \text{Co}, \text{Ru}, \text{and Rh}$ ), *Phys. Rev. B* **88**, 155122 (2013).
- [10] Y. Otomo, K. Iwasa, K. Suyama, K. Tomiyasu, H. Sagayama, R. Sagayama, H. Nakao, R. Kumai, and Y. Murakami, Chiral crystal-structure transformation of  $R_3\text{Co}_4\text{Sn}_{13}$  ( $R = \text{La}$  and  $\text{Ce}$ ), *Phys. Rev. B* **94**, 075109 (2016).
- [11] J. Welsch, S. Ramakrishnan, C. Eisele, N. van Well, A. Schönleber, S. van Smaalen, S. Mattheppanavar, A. Thamizhavel, M. Tolkieln, C. Paulmann, and S. Ramakrishnan, Second-order charge-density-wave transition in single crystals of  $\text{La}_3\text{Co}_4\text{Sn}_{13}$ , *Phys. Rev. Materials* **3**, 125003 (2019).
- [12] S. Ramakrishnan and S. van Smaalen, Unusual ground states in  $R_5\text{T}_4\text{X}_{10}$  ( $R = \text{rare earth}; T = \text{Rh}, \text{Ir}; \text{and } X = \text{Si}, \text{Ge}, \text{Sn}$ ): a review, *Rep. Prog. Phys.* **80**, 116501 (2017).
- [13] D. E. Bugaris, C. D. Malliakas, F. Han, N. P. Calta, M. Sturza, M. J. Krogstad, R. Osborn, S. Rosenkranz, J. P. C. Ruff, G. Trimarchi, S. L. Bud'ko, M. Balasubramanian, D. Y. Chung, and M. G. Kanatzidis, Charge density wave in the new polymorphs of  $\text{RE}_2\text{Ru}_3\text{Ge}_5$  ( $\text{RE} = \text{Pr}, \text{Sm}, \text{Dy}$ ), *J. Amer. Chem. Soc.* **139**, 4130 (2017).
- [14] C. N. Kuo, C. J. Hsu, C. W. Tseng, W. T. Chen, S. Y. Lin, W. Z. Liu, Y. K. Kuo, and C. S. Lue, Charge density wave like behavior with magnetic ordering in orthorhombic  $\text{Sm}_2\text{Ru}_3\text{Ge}_5$ , *Phys. Rev. B* **101**, 155140 (2020).

- [15] K. K. Kolincio, M. Roman, and T. Klimczuk, Enhanced mobility and large linear nonsaturating magnetoresistance in the magnetically ordered states of  $\text{TmNiC}_2$ , *Phys. Rev. Lett.* **125**, 176601 (2020).
- [16] M. Roman, M. Fritthum, B. Stöger, D. T. Adroja, and H. Michor, Charge density wave and crystalline electric field effects in  $\text{TmNiC}_2$ , *Phys. Rev. B* **107**, 125137 (2023).
- [17] S. Ramakrishnan, A. Schönleber, J.-K. Bao, T. Rekis, S. R. Kotla, A. M. Schaller, S. van Smaalen, L. Noohinejad, M. Tolkieln, C. Paulmann, N. S. Sangeetha, D. Pal, A. Thamizhavel, and S. Ramakrishnan, Modulated crystal structure of the atypical charge density wave state of single-crystal  $\text{Lu}_2\text{Ir}_3\text{Si}_5$ , *Phys. Rev. B* **104**, 054116 (2021).
- [18] S. Ramakrishnan, A. Schönleber, T. Rekis, N. van Well, L. Noohinejad, S. van Smaalen, M. Tolkieln, C. Paulmann, B. Bag, A. Thamizhavel, D. Pal, and S. Ramakrishnan, Unusual charge density wave transition and absence of magnetic ordering in  $\text{Er}_2\text{Ir}_3\text{Si}_5$ , *Phys. Rev. B* **101**, 060101(R) (2020).
- [19] S. Ramakrishnan, J. Bao, C. Eisele, B. Patra, M. Nohara, B. Bag, L. Noohinejad, M. Tolkieln, C. Paulmann, A. M. Schaller, T. Rekis, S. R. Kotla, A. Schönleber, A. Thamizhavel, B. Singh, S. Ramakrishnan, and S. van Smaalen, Coupling between charge density wave ordering and magnetism in  $\text{Ho}_2\text{Ir}_3\text{Si}_5$ , *Chem. Mater.* **35**, 1980 (2023).
- [20] L. Zeng, X. Hu, N. Wang, J. Sun, P. Yang, M. Boubeche, S. Luo, Y. He, J. Cheng, D.-X. Yao, and H. Luo, Interplay between charge-density-wave, superconductivity, and ferromagnetism in  $\text{CuIr}_{2-x}\text{Cr}_x\text{Te}_4$  chalcogenides, *J. Phys. Chem. Lett.* **13**, 2442 (2022).
- [21] Z. Guguchia, C. Mielke, D. Das, R. Gupta, J.-X. Yin, H. Liu, Q. Yin, M. H. Christensen, Z. Tu, C. Gong, N. Shumiya, M. S. Hossain, T. Gamsakhurdashvili, M. Elender, P. Dai, A. Amato, Y. Shi, H. C. Lei, R. M. Fernandes, M. Z. Hasan, H. Luetkens, and R. Khasanov, Tunable unconventional kagome superconductivity in charge ordered  $\text{RbV}_3\text{Sb}_5$  and  $\text{KV}_3\text{Sb}_5$ , *Nature Commun.* **14**, 153 (2023).
- [22] L. Kautzsch, B. R. Ortiz, K. Mallayya, J. Plumb, G. Pokharel, J. P. C. Ruff, Z. Islam, E.-A. Kim, R. Seshadri, and S. D. Wilson, Structural evolution of the kagome superconductors  $\text{AV}_3\text{Sb}_5$  ( $A = \text{K}, \text{Rb}, \text{and Cs}$ ) through charge density wave order, *Phys. Rev. Mater.* **7**, 024806 (2023).
- [23] Q. Xiao, Y. Lin, Q. Li, X. Zheng, S. Francoual, C. Plueckthun, W. Xia, Q. Qiu, S. Zhang, Y. Guo, J. Feng, and Y. Peng, Coexistence of multiple stacking charge density waves in kagome

- superconductor CsV<sub>3</sub>Sb<sub>5</sub>, Phys. Rev. Res. **5**, L012032 (2023).
- [24] X. Zhou, Y. Li, X. Fan, J. Hao, Y. Xiang, Z. Liu, Y. Dai, Z. Wang, Y. Yao, and H.-H. Wen, Electronic correlations and evolution of the charge density wave in the kagome metals AV<sub>3</sub>Sb<sub>5</sub> (A = K, Rb, and Cs), Phys. Rev. B **107**, 165123 (2023).
- [25] Y. Wang, T. Wu, Z. Li, K. Jiang, and J. Hu, Structure of the kagome superconductor CsV<sub>3</sub>Sb<sub>5</sub> in the charge density wave state, Phys. Rev. B **107**, 184106 (2023).
- [26] K. Yang, W. Xia, X. Mi, L. Zhang, Y. Gan, A. Wang, Y. Chai, X. Zhou, X. Yang, Y. Guo, and M. He, Charge fluctuations above  $t_{CDW}$  revealed by glasslike thermal transport in kagome metals AV<sub>3</sub>Sb<sub>5</sub> (A = K, Rb, and Cs), Phys. Rev. B **107**, 184506 (2023).
- [27] X. Teng, L. Chen, F. Ye, E. Rosenberg, Z. Liu, J.-X. Yin, Y.-X. Jiang, J. S. Oh, M. Z. Hasan, K. J. Neubauer, B. Gao, Y. Xie, M. Hashimoto, D. Lu, C. Jozwiak, A. Bostwick, E. Rotenberg, R. J. Birgeneau, J.-H. Chu, M. Yi, and P. Dai, Discovery of charge density wave in a kagome lattice antiferromagnet, Nature **609**, 490 (2022).
- [28] X. Teng, J. S. Oh, H. Tan, L. Chen, J. Huang, B. Gao, J.-X. Yin, J.-H. Chu, M. Hashimoto, D. Lu, C. Jozwiak, A. Bostwick, E. Rotenberg, G. E. Granroth, B. Yan, R. J. Birgeneau, P. Dai, and M. Yi, Magnetism and charge density wave order in kagome FeGe, Nat. Phys. **19** (2023).
- [29] H. Zhou, S. Yan, D. Fan, D. Wang, and X. Wan, Magnetic interactions and possible structural distortion in kagome FeGe from first-principles calculations and symmetry analysis, Phys. Rev. B **108**, 035138 (2023).
- [30] U. Haussermann, S. Amerioun, L. Eriksson, C.-S. Lee, and G. J. Miller, The  $s$ - $p$  bonded representatives of the prominent BaAl<sub>4</sub> structure type: A case study on structural stability of polar intermetallic network structures, J. Amer. Chem. Soc. **124**, 4371 (2002).
- [31] M. Stavinoha, J. A. Cooley, S. G. Minasian, T. M. McQueen, S. M. Kauzlarich, C.-L. Huang, and E. Morosan, Charge density wave behavior and order-disorder in the antiferromagnetic metallic series Eu(Ga<sub>1-x</sub>Al<sub>x</sub>)<sub>4</sub>, Phys. Rev. B **97**, 195146 (2018).
- [32] K. Wang, R. Mori, Z. Wang, L. Wang, J. H. S. Ma, D. W. Latzke, D. E. Graf, J. D. Denlinger, D. Campbell, B. A. Bernevig, A. Lanzara, and J. Paglione, Crystalline symmetry-protected non-trivial topology in prototype compound BaAl<sub>4</sub>, NPJ Quant. Mater. **6**, 28 (2021).
- [33] T. Shang, Y. Xu, D. J. Gawryluk, J. Z. Ma, T. Shiroka, M. Shi, and E. Pomjakushina, Anomalous hall resistivity and possible topological hall effect in the EuAl<sub>4</sub> antiferromagnet,

- Phys. Rev. B **103**, L020405 (2021).
- [34] R. Mori, K. Wang, T. Morimoto, S. Ciocys, J. D. Denlinger, J. Paglione, and A. Lanzara, Observation of a flat and extended surface state in a topological semimetal, *Materials* **15** (2022).
- [35] M. Gen, R. Takagi, Y. Watanabe, S. Kitou, H. Sagayama, N. Matsuyama, Y. Kohama, A. Ikeda, Y. Onuki, T. Kurumaji, T.-h. Arima, and S. Seki, Rhombic skyrmion lattice coupled with orthorhombic structural distortion in  $\text{EuAl}_4$ , *Phys. Rev. B* **107**, L020410 (2023).
- [36] L.-L. Wang, N. K. Nepal, and P. C. Canfield, Origin of charge density wave in topological semimetals  $\text{SrAl}_4$  and  $\text{EuAl}_4$  (2023), arXiv:2306.15068 [cond-mat.mtrl-sci].
- [37] A. Nakamura, T. Uejo, F. Honda, T. Takeuchi, H. Harima, E. Yamamoto, Y. Haga, K. Matsubayashi, Y. Uwatoko, M. Hedo, T. Nakama, and Y. Ōnuki, Transport and magnetic properties of  $\text{EuAl}_4$  and  $\text{EuGa}_4$ , *J. Phys. Soc. Jpn* **84**, 124711 (2015).
- [38] S. Shimomura, H. Murao, S. Tsutsui, H. Nakao, A. Nakamura, M. Hedo, T. Nakama, and Y. Ōnuki, Lattice modulation and structural phase transition in the antiferromagnet  $\text{EuAl}_4$ , *J. Phys. Soc. Jpn* **88**, 014602 (2019).
- [39] K. Kaneko, T. Kawasaki, A. Nakamura, K. Munakata, A. Nakao, T. Hanashima, R. Kiyonagi, T. Ohhara, M. Hedo, T. Nakama, and Y. Ōnuki, Charge-density-wave order and multiple magnetic transitions in divalent europium compound  $\text{EuAl}_4$ , *J. Phys. Soc. Jpn* **90**, 064704 (2021).
- [40] S. Ramakrishnan, S. R. Kotla, T. Rekiş, J.-K. Bao, C. Eisele, L. Noohinejad, M. Tolkieln, C. Paulmann, B. Singh, R. Verma, B. Bag, R. Kulkarni, A. Thamizhavel, B. Singh, S. Ramakrishnan, and S. van Smaalen, Orthorhombic charge density wave on the tetragonal lattice of  $\text{EuAl}_4$ , *IUCrJ* **9**, 378 (2022).
- [41] W. R. Meier, J. R. Torres, R. P. Hermann, J. Zhao, B. Lavina, B. C. Sales, and A. F. May, Thermodynamic insights into the intricate magnetic phase diagram of  $\text{EuAl}_4$ , *Phys. Rev. B* **106**, 094421 (2022).
- [42] R. Takagi, N. Matsuyama, V. Ukleev, L. Yu, J. S. White, S. Francoual, J. R. L. Mardegan, S. Hayami, H. Saito, K. Kaneko, K. Ohishi, Y. Ōnuki, T.-h. Arima, Y. Tokura, T. Nakajima, and S. Seki, Square and rhombic lattices of magnetic skyrmions in a centrosymmetric binary compound, *Nature Commun.* **13**, 1472 (2022).
- [43] K. Kaneko, M. D. Frontzek, M. Matsuda, A. Nakao, K. Munakata, T. Ohhara, M. Kakihana,

- Y. Haga, M. Hedo, T. Nakama, and Y. Onuki, Unique helical magnetic order and field-induced phase in trillium lattice antiferromagnet EuPtSi, *J. Phys. Soc. Jpn* **88**, 013702 (2019).
- [44] Y. Onuki, M. Hedo, and F. Honda, Unique electronic states of Eu-based compounds, *J. Phys. Soc. Jpn* **89**, 102001 (2020).
- [45] X. Y. Zhu, H. Zhang, D. J. Gawryluk, Z. X. Zhen, B. C. Yu, S. L. Ju, W. Xie, D. M. Jiang, W. J. Cheng, Y. Xu, M. Shi, E. Pomjakushina, Q. F. Zhan, T. Shiroka, and T. Shang, Spin order and fluctuations in the EuAl<sub>4</sub> and EuGa<sub>4</sub> topological antiferromagnets: A  $\mu$ SR study, *Phys. Rev. B* **105**, 014423 (2022).
- [46] A. Nakamura, T. Uejo, H. Harima, S. Araki, T. C. Kobayashi, M. Nakashima, Y. Amako, M. Hedo, T. Nakama, and Y. Onuki, Characteristic fermi surfaces and charge density wave in SrAl<sub>4</sub> and related compounds with the BaAl<sub>4</sub>-type tetragonal structure, *J. Alloys Compounds* **654**, 290 (2016).
- [47] H. Niki, H. Kuroshima, N. Higa, M. Morishima, M. Yogi, A. Nakamura, K. Niki, T. Maehira, M. Hedo, T. Nakama, and Y. Onuki, NMR study of characteristic CDW transition in SrAl<sub>4</sub>, *Proc. Int'l Conf. Strongly Correlated Electron Systems (SCES2019)* (2020).
- [48] G. J. Miller, F. Li, and H. F. Franzen, The structural phase transition in calcium-aluminum compound (CaAl<sub>4</sub>): a concerted application of landau theory and energy band theory, *J. Amer. Chem. Soc.* **115**, 3739 (1993).
- [49] M. Kobata, S.-i. Fujimori, Y. Takeda, T. Okane, Y. Saitoh, K. Kobayashi, H. Yamagami, A. Nakamura, M. Hedo, T. Nakama, and Y. Onuki, Electronic structure of EuAl<sub>4</sub> studied by photoelectron spectroscopy, *J. Phys. Soc. Jpn* **85**, 094703 (2016).
- [50] Z. Jiliang and B. Svilen, Synthesis, structural characterization and properties of SrAl<sub>4-x</sub>Ge<sub>x</sub>, BaAl<sub>4-x</sub>Ge<sub>x</sub>, and EuAl<sub>4-x</sub>Ge<sub>x</sub> ( $x \approx 0.3 - 0.4$ ) – rare examples of electron-rich phases with the BaAl<sub>4</sub> structure type, *J. Sol. State Chem.* **205**, 21 (2013).
- [51] A. Zevalkink, M. Bobnar, U. Schwarz, and Y. Grin, Making and breaking bonds in superconducting SrAl<sub>4-x</sub>Si<sub>x</sub> ( $0 \leq x \leq 2$ ), *Chem. Mater.* **29**, 1236 (2017).
- [52] C. Paulmann, P24ToolsCP, v1.12, software tools for postprocessing area detector, x-ray diffraction data (2022).
- [53] See Supplemental Material at [URL will be inserted by publisher] for details on the diffraction experiments and values of the structural parameters, including the citation [81].
- [54] A. M. M. Schreurs, X. Xian, and L. M. J. Kroon-Batenburg, EVAL15: a diffraction data

- integration method based on ab initio predicted profiles, *J. Appl. Crystallogr.* **43**, 70 (2010).
- [55] G. M. Sheldrick, *SADABS, Version 2008/1* (Göttingen: University of Göttingen, 2008).
- [56] V. Petricek, M. Dusek, and L. Palatinus, Crystallographic computing system JANA2006: general features, *Z. Kristallogr.* **229**, 345 (2014).
- [57] V. Petricek, V. Eigner, M. Dusek, and A. Cejchan, Discontinuous modulation functions and their application for analysis of modulated structures with the computing system JANA2006, *Z. Kristallogr.* **231**, 301 (2016).
- [58] H. T. Stokes, B. J. Campbell, and S. van Smaalen, Generation of  $(3+d)$ -dimensional superspace groups for describing the symmetry of modulated crystalline structures, *Acta Crystallogr. A* **67**, 45 (2011).
- [59] G. Kresse and J. Furthmüller, Efficient iterative schemes for ab initio total-energy calculations using a plane-wave basis set, *Phys. Rev. B* **54**, 11169 (1996).
- [60] P. E. Blöchl, Projector augmented-wave method, *Phys. Rev. B* **50**, 17953 (1994).
- [61] G. Kresse and D. Joubert, From ultrasoft pseudopotentials to the projector augmented-wave method, *Phys. Rev. B* **59**, 1758 (1999).
- [62] J. P. Perdew, K. Burke, and M. Ernzerhof, Generalized gradient approximation made simple, *Phys. Rev. Lett.* **77**, 3865 (1996).
- [63] Q. Wu, S. Zhang, H.-F. Song, M. Troyer, and A. A. Soluyanov, Wanniertools: An open-source software package for novel topological materials, *Computer Physics Communications* **224**, 405 (2018).
- [64] A. A. Mostofi, J. R. Yates, Y.-S. Lee, I. Souza, D. Vanderbilt, and N. Marzari, wannier90: A tool for obtaining maximally-localised wannier functions, *Computer Physics Communications* **178**, 685 (2008).
- [65] A. A. Mostofi, J. R. Yates, G. Pizzi, Y.-S. Lee, I. Souza, D. Vanderbilt, and N. Marzari, An updated version of wannier90: A tool for obtaining maximally-localised wannier functions, *Computer Physics Communications* **185**, 2309 (2014).
- [66] N. Marzari, A. A. Mostofi, J. R. Yates, I. Souza, and D. Vanderbilt, Maximally localized wannier functions: Theory and applications, *Rev. Mod. Phys.* **84**, 1419 (2012).
- [67] P. Giannozzi, S. de Gironcoli, P. Pavone, and S. Baroni, Ab initio calculation of phonon dispersions in semiconductors, *Phys. Rev. B* **43**, 7231 (1991).
- [68] X. Gonze and C. Lee, Dynamical matrices, born effective charges, dielectric permittivity

- tensors, and interatomic force constants from density-functional perturbation theory, *Phys. Rev. B* **55**, 10355 (1997).
- [69] A. Togo and I. Tanaka, First principles phonon calculations in materials science, *Scripta Materialia* **108**, 1 (2015).
- [70] P. Giannozzi, S. Baroni, N. Bonini, M. Calandra, R. Car, C. Cavazzoni, D. Ceresoli, G. L. Chiarotti, M. Cococcioni, I. Dabo, A. D. Corso, S. de Gironcoli, S. Fabris, G. Fratesi, R. Gebauer, U. Gerstmann, C. Gougoussis, A. Kokalj, M. Lazzeri, L. Martin-Samos, N. Marzari, F. Mauri, R. Mazzarello, S. Paolini, A. Pasquarello, L. Paulatto, C. Sbraccia, S. Scandolo, G. Sclauzero, A. P. Seitsonen, A. Smogunov, P. Umari, and R. M. Wentzcovitch, Quantum espresso: a modular and open-source software project for quantum simulations of materials, *J. Phys.: Condens. Matter* **21**, 395502 (2009).
- [71] P. Giannozzi, O. Andreussi, T. Brumme, O. Bunau, M. B. Nardelli, M. Calandra, R. Car, C. Cavazzoni, D. Ceresoli, M. Cococcioni, N. Colonna, I. Carnimeo, A. D. Corso, S. de Gironcoli, P. Delugas, R. A. DiStasio, A. Ferretti, A. Floris, G. Fratesi, G. Fugallo, R. Gebauer, U. Gerstmann, F. Giustino, T. Gorni, J. Jia, M. Kawamura, H.-Y. Ko, A. Kokalj, E. Küçükbenli, M. Lazzeri, M. Marsili, N. Marzari, F. Mauri, N. L. Nguyen, H.-V. Nguyen, A. O. de-la Roza, L. Paulatto, S. Poncé, D. Rocca, R. Sabatini, B. Santra, M. Schlipf, A. P. Seitsonen, A. Smogunov, I. Timrov, T. Thonhauser, P. Umari, N. Vast, X. Wu, and S. Baroni, Advanced capabilities for materials modelling with quantum espresso, *J. Phys.: Condens. Matter* **29**, 465901 (2017).
- [72] Rigaku, CrysAlis pro version 171.40.53, rigaku oxford diffraction. (2019).
- [73] E. Parthé, B. Chabot, H. F. Braun, and N. Engel, Ternary BaAl<sub>4</sub>-type derivative structures, *Acta Crystallogr. B* **39**, 588 (1983).
- [74] K. Momma and F. Izumi, VESTA: a three-dimensional visualization system for electronic and structural analysis, *J. Appl. Crystallogr.* **41**, 653 (2008).
- [75] S. van Smaalen, *Incommensurate Crystallography* (Oxford University Press, Oxford, 2007).
- [76] Y. Liu, C. Li, J. Wang, D. Yin, J. Shi, and R. Xiong, Thermal transport properties and electronic structure of W-doped rubidium blue bronzes Rb<sub>0.3</sub>Mo<sub>1-x</sub>W<sub>x</sub>O<sub>3</sub> (x = 0, 0.001, 0.003, 0.005), *Physica B* **405**, 2857 (2010).
- [77] D. Yan, L. Zeng, Y. Lin, J. Yin, Y. He, X. Zhang, M. Huang, B. Shen, M. Wang, Y. Wang, D. Yao, and H. Luo, Superconductivity in Ru-doped CuIr<sub>2</sub>Te<sub>4</sub> telluride chalcogenide, *Phys.*

- Rev. B **100**, 174504 (2019).
- [78] J. Gao, Q. Wu, C. Persson, and Z. Wang, Irvsp: To obtain irreducible representations of electronic states in the VASP, *Computer Physics Communications* **261**, 107760 (2021).
- [79] M. D. Johannes and I. I. Mazin, Fermi surface nesting and the origin of charge density waves in metals, *Phys. Rev. B* **77**, 165135 (2008).
- [80] H. Suzuki, A. Inaba, and C. Meingast, Accurate heat capacity data at phase transitions from relaxation calorimetry, *Cryogenics* **50**, 693 (2010).
- [81] S. Parsons, Introduction to twinning, *Acta Crystallogr. D* **59**, 1995 (2003).